DLSU Research Congress 2022
De La Salle University, Manila, Philippines
July 6 to 8, 2022

Simulated characteristics of a compact phased dual-band patch antenna array for use in body-contact radar imaging

Alfonso Vicente L. Jadie[1*], Romeric F. Pobre[1]
[1]*Optics Research Unit, CENSER and Department of Physics*
College of Science, De la Salle University - Manila
**alfonso_vicente_jadie@dlsu.edu.ph*

Abstract: The unidirectional scanning performance of a 2-element phased array of dual-band patch antennas was simulated using finite-element-method modeling software in order to assess its viability as an antenna architecture for body-contact wideband radar imaging. The simulated antenna element has a maximum realized gain of 1.87 at 2.52 GHz and a polarization ellipticity below 0.17 from 2-3GHz, but the reflection coefficient magnitude is not low enough to establish a -10dB impedance bandwidth in the desired frequency range. The researchers also identified a nonviable band of frequencies from 2.06-2.14 GHz close to the lower resonance frequency wherein the radiation pattern of the individual elements deviates from unidirectionality along the normal of the patch face. The researchers also estimated the array to have an effective angular scanning range of 60°, with the primary limiting factor as susceptibility to external noise from directions opposite the patch face for large degrees of inter-element phase shift.

Key Words: finite element method antenna simulation, phased array, dual-band patch antenna

1. INTRODUCTION

Among current research interests in healthcare technology is the development of continuous health monitoring systems that are non-invasive, cost-effective to manufacture and implement, and allow the patient greater freedom to perform regular activities while under observation. One particular area of interest is the use of radio-frequency (RF) waves for monitoring cardiac and respiratory activity through movement, applicable in low-cost, portable systems capable of detecting transient symptoms over long-term monitoring.

Recent developments of RF-based health monitoring technology include wideband radar-based monitoring of arterial pulse activity (Lauteslager, Tommer, Lande, & Constandinou, 2019), vital signs detection of multiple targets via frequency-modulated continuous-wave radar (Wang, Shui, Yang, Li, & Wang, 2021) and wearable RF monitors for heart rate, respiratory rate and respiratory volume (Sharma, Hui, Zhou, Conroy, & Kan, 2020).

This report is part of a larger study that seeks to build on a previous study on body-contact radar imaging of the heart and surrounding tissue by (Brovoll, et al., 2014) using wideband radar via an 8-element linear array of wideband antennas capable of being switched between transmitting (TX) and receiving (RX) mode. In the study by (Brovoll, et al., 2014), the distance of signal-reflective regions from each TX-RX pair in the array is obtained via inverse Fourier transform of the signal data from the frequency domain to the travel time/distance domain, while the angular coordinates of the reflective regions are obtained by a back-projection-based technique of summing the contributions of individual TX-RX pairs to the total image.

This report investigates an alternative radar architecture for the imaging methodology used by (Brovoll, et al., 2014). In particular, the researchers' ongoing study investigates the viability of obtaining similar imaging capability with a system composed of a single TX element plus a phased scanning array of a few RX elements, thus reducing both the physical array size and the complexity of the radar circuitry. This report presents the simulation results of a two-

element phased array of wideband patch antennas for intended use in body-contact radar imaging, as a part of this wider research aim.

1.1 Background theory

It is explained in (Balanis, 2016) that in the far-field region, the total electric field magnitude $|\vec{E}_{total}(\vec{r})|$ produced by a transmitting array of identical antenna elements located at the origin of a given coordinate system can be modeled in terms of the electric field $|\vec{E}_{element}(\vec{r})|$ of an individual element located at the origin, multiplied by the array factor $F_{array}(\hat{r})$ associated with that particular array, such that

$$\left|\vec{E}_{total}(\vec{r})\right| = |\vec{E}_{element}(\vec{r})|F_{array}(\hat{r}) \qquad \text{(Eq. 1)}$$

where the form of $F_{array}(\hat{r})$ is generally dictated by the number of elements in the array and their relative positions, input signal magnitudes and input phases relative to each other. A sufficiently designed array of transmitting elements can thus be made to aim its maximum radiated output in a particular direction $\hat{r}_0$ by electronically varying the relative phases and amplitude contributions of the individual elements; in a similar manner, an equivalent array of receiving elements can be electronically oriented so that its maximum directional sensitivity is to signals incoming from a given direction $\hat{r}_0$.

As shown by (Balanis, 2016), for the specific case of a uniform linear array or ULA (a linear array of elements with uniform spacing D_{ARRAY} between elements, uniform contributions in signal amplitude and uniform phase difference $\Delta\phi_{signal}$ between contributions of adjacent elements), the array factor is azimuthally symmetric about the axis of the array and can be expressed in the form

$$F_{array}(\theta_n) = \frac{\sin[0.5N\Psi(\theta_n)]}{\sin[0.5\Psi(\theta_n)]} \qquad \text{(Eq. 2)}$$

where

N = number of elements

θ_n = angle of direction of outbound radiation relative to the normal of the ULA axis

$\Psi(\theta_n)$ = $kD_{ARRAY}\sin\theta_n + \Delta\phi_{signal}$ = phase difference in the far-field between radio waves from adjacent elements traveling at angle θ_{normal}

k = wavenumber of the radiation in the medium of wave propagation

where the sign conventions of θ_n and $\Delta\theta_{signal}$ are given by Fig. 1.

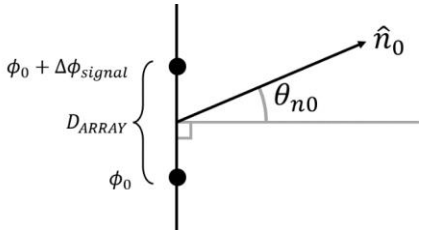

Figure 1: Diagram of phased array with sign conventions for θ_n, $\Delta\phi_{signal}$

As shown in (Balanis, 2016), the array factor $F_{array}(\theta_n)$ of a ULA can be steered so that the direction $\hat{n}_0$ of its maximum value lies at a given angle θ_{n0} by setting the phase difference $\Delta\phi_{signal}$ between successive elements to $\Delta\phi_{signal} = -kD_{ARRAY}\sin\theta_{n0}$, so that the emitted waves traveling at the angle θ_{n0} interfere constructively in the far-field region with

$$\Psi(\theta_{n0}) = kD_{ARRAY}\sin\theta_{n0} + \Delta\phi_{signal} = 0 \qquad \text{(Eq. 3)}$$

2. METHODOLOGY

2.1 Simulation procedure

The simulation of the array system was accomplished via the physics modeling software COMSOL Multiphysics, in which finite-element discretization methods are used to obtain values for the amplitude and phase of a sinusoidally-oscillating electric field within the volume of the model that fulfill approximate consistency with Maxwell's equations along with the boundary conditions imposed within the model.

In the geometry of the simulation (example shown in Fig. 2), the component (either the entire 2-antenna array, or an individual element) to be analyzed is centered within a spherical volume assigned with the material properties of the surrounding medium (air/free space, (σ = 0. S/m, ϵ_r = 1, μ_r = 1)), where a scattering boundary condition is imposed on the surface of the sphere so that the radially-propagating component of any transmitted waves vanish at the artificial boundary instead of reflecting; this way, the simulated electric field approximates that of a wave propagating into infinite space.

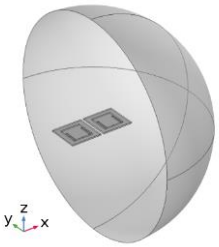

Figure 2: Example 3D geometry of COMSOL model, enclosing surface partly removed for clarity

Each antenna element is modeled as a square block of thickness ($d_{dielectric}$ = 1.6 mm) and material properties (σ = 0.004 S/m, ϵ_r = 4.5, μ_r = 1) of a typical commercial FR4 fiberglass PCB, with one face occupied by a ground plane and the opposite face containing the antenna trace placed in the center of the PCB. The copper traces of the antenna are represented as a boundary condition on the appropriate surfaces representing them as perfect electrical conductors. Finally, between the feed point and ground plane of each element, a 1V driving voltage is applied along a 2D strip of negligible width (< 1 mm) representing a connection to a typical 50 ohm-impedance SMA transmission line.

2.2 Antenna element and array geometry

The design of the basis element for the antennas is based on microstrip patch antennas, which are well-suited as a test element for the body-contact radar array because of their flat shape and relative ease of fabrication from commercial printed circuit board (PCB) substrate. To facilitate an increased bandwidth, shape modifications need to be applied to the basic rectangular shape of the patch; a relatively simple method is reported by (Yang, Zhang, Ye, & Rahmat-Samii, 2001) and (Patel & Kosta, 2011) in which a pair of parallel slots are added to the patch to add an additional resonance frequency, which couples with the original resonance frequency to form a wider operating bandwidth.

As reported by (Brovoll, et al., 2013), a suggested preliminary frequency range for body-contact radar applications is 2-3 GHz, a frequency range low enough to avoid significant attenuation but high enough that the signal response was independent of the antenna dimension used in the original study (the original study was carried out using various sizes of bowtie antennas). Within this 2-3GHz range, the modified patch for this study is tuned for resonant frequencies of 2.1 and 2.5 GHz.

The shape parameters of the patch are shown below in Fig. 3 and Table 1, with the ground plane side length L_{GND}, slot width W_{SLOT} and feed point distance from the patch edge Y_{FEED} arbitrarily chosen as 40mm, 1mm and 1mm respectively and the remaining parameters chosen by comparing multiple iterations of the design with 1mm increments in variation. The square patch length L_{PATCH} was chosen based on the best impedance match with the feed port for a basic patch without slots at 2.5GHz, while the slot length L_{SLOT} and off-center-axis displacement X_{SLOT} of the slots were chosen based on the best impedance match at 2.1 GHz. The full 2-antenna array consists of 2 elements spaced an arbitrary but close-spaced distance $D_{ARRAY} = 1.1L_{GND}$ apart for compactness, oriented such that the polarization of the antennas (which is parallel to the slots) is perpendicular to the array axis; the radiation pattern of the full array is simulated for various values of phase difference $\Delta\phi_{signal}$ from 0 to 180 degrees imposed between the driving voltages of the two elements.

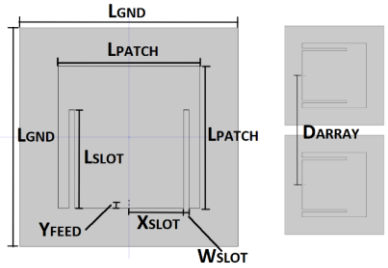

Figure 3: Features of antenna element and array geometry (pre-optimization)

Table 1: Shape parameters of array and optimized antenna elements

Shape parameter	Value
D_{ARRAY}	44 mm
L_{GND}	40 mm
Y_{FEED}	1 mm
W_{SLOT}	1 mm
L_{PATCH}	27 mm
L_{SLOT}	18 mm
X_{SLOT}	11 mm

3. RESULTS AND DISCUSSION

3.1 Frequency-domain characteristics of antenna element

The primary selection criterion for the shape parameters of the antenna element is the extent of impedance matching between the antenna and the 50 ohm feed point; impedance mismatch leads to inefficiencies in signal transmission/reception due to partial reflection of signals from the mismatched connection. The efficiency of signal passage through an impedance mismatch can be quantified in terms of the voltage reflection coefficient $R_{REF} = V_R/V_I$ defined as the ratios in amplitude of the reflected signal voltage V_R over the incident signal voltage V_I; the shape parameters of the array element are chosen to minimize R_{REF} at the resonant frequencies. A common definition for the impedance bandwidth of an antenna is the frequency range within which $R_{ref} \leq 0.1 = -10dB$ (Yang, Zhang, Ye, & Rahmat-Samii, 2001), (Patel & Kosta, 2011).

The antenna design must also be constrained to have an acceptable radiation pattern. The radiation pattern of an antenna is often described in terms of its radiation intensity $U_{rad}(\hat{r})$, which denotes the distribution of the radiated power per solid-angle in the far-field and is related to the electric field $\vec{E}_{far}(\vec{r})$ in the far-field region by $U_{rad}(\hat{r}) \propto r^2\left|\vec{E}_{far}(\vec{r})\right|^2$. For the purposes of this application it is ideal that the radiation pattern of the individual element be mainly broadside-directed, such that the maximum of $U_{rad}(\hat{r})$) be oriented along the normal $\hat{n}_{ant}$ of the patch-antenna face of the PCB while $U_{rad}(\hat{r})$ in the directions away from the opposite face of the PCB are negligible. These two properties can be quantified in terms of ratios $R_{broadside}$ and R_{back} respectively, where

$$R_{broadside} \approx \left(\frac{\left|\vec{E}_S(\hat{r} = \hat{n}_{ant})\right|}{\max_S\left(\left|\vec{E}_S(\hat{r})\right|\right)}\right)^2 \quad \text{(Eq. 4)}$$

$$R_{back} \approx \left(\frac{\max_S\left(\left|\vec{E}_S(\hat{r} \cdot \hat{n}_{ant} \leq 0)\right|\right)}{\max_S\left(\left|\vec{E}_S(\hat{r})\right|\right)}\right)^2 \quad \text{(Eq. 5)}$$

Where

$\vec{E}_S$ = electric field on the surface of the sphere enclosing the antenna element in the simulation, as shown in Fig. 2

$\max_S()$ = function denoting the maximum value of the argument within the surface of the enclosing sphere

It is desirable for the antenna design that $R_{broadside} \approx 1$, while $R_{back} \ll 1$. The matching efficiency and radiation pattern quality can further be quantified in terms of the realized gain $G_{real}(\hat{r})$, denoting the amount of radiation intensity along $\hat{r}$ relative to that of a perfectly-efficient isotropic radiator with the same input power. Finally, an additional characteristic of note is the polarization ellipticity $e_{rad} = E_{minor}/E_{major}$, where E_{minor} and E_{major} denote the components of the electric field amplitude along the minor and major elliptical axes of the trajectory traced by the electric field vector in the plane normal to the wave vector.

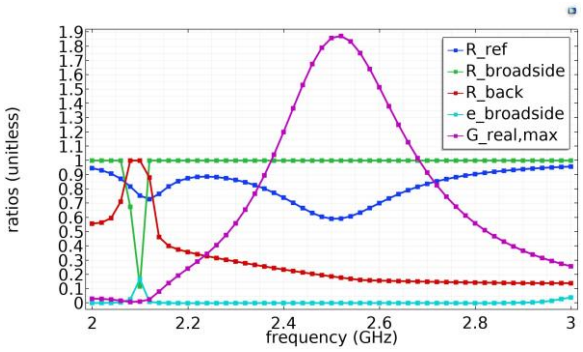

Figure 4: Frequency-domain characteristics of various antenna element parameters from 2-3 GHz; domain resolution = 20 MHz.

Figure 4 shows the frequency-domain characteristics in the 2-3GHz range for the voltage reflection coefficient R_{REF}, as well as $R_{broadside}$, R_{back}, the ellipticity $e_{broadside}$ along the intended main radiation direction, and the maximum value $G_{real,max}$ of the realized gain across all directions. The consistent low value of $e_{broadside} < 0.17$ from 2-3 GHz indicates the broadside radiation is mainly linearly-polarized. The graph of R_{REF} illustrates that the resonant frequencies of the element are approximately 2.12 GHz and 2.5-2.52 GHz, close to the initial goals of 2.1 GHz and 2.5 GHz; however, the minimum of R_{REF} is approximately $0.59 \approx -2.29\,dB$, outside of the $-10dB$ threshold for a viable impedance bandwidth. Additionally, at frequencies close to the lower resonance the radiation pattern is non-ideal; within the 2.06-2.14 GHz range is a significant drop in $R_{broadside}$ and a spike in R_{back} indicating the radiation pattern in this frequency band deviates from the

desired characteristics of primarily broadside radiation. This is supported by the characteristics of the maximum realized gain $G_{real,max}$, which reaches a peak of $G_{real,max} = 1.87$ at 2.52 GHz but has no corresponding peak at 2.1 GHz; therefore this band within 2.06-2.14 GHz is considered to be excluded from the viable range for the purposes of this array.

3.2 Characteristics of array radiation pattern

This section presents the 2D radiation pattern of the array for various operating frequencies and degrees of phase shift $\Delta\phi_{signal}$ between elements, in the plane containing the desired radar image to be captured (equivalent to the plane of the 2D diagram in Fig.1 or the X-Z plane in the 3D diagram in Fig. 2). The radiation pattern of the array was simulated for frequencies from 2.2-2.6 GHz in 0.1GHz increments, and for phase shifts from 0° to +180° in 15° increments.

The radiation patterns take the form of polar plots with respect to the broadside direction of the value $U_{rad,n}(\hat{r})$ of the radiation intensity $U_{rad}(\hat{r})$ normalized with respect to its maximum value across all directions $\max_s(U_{rad}(\hat{r}))$, expressed as

$$\mathrm{U_{rad,n}}(\hat{r}) = \frac{U_{rad}(\hat{r})}{\max_s(U_{rad}(\hat{r}))} \qquad \text{(Eq. 6)}$$

Note that the given value of maximum radiation intensity $\max_s(U_{rad}(\hat{r}))$ in Eq. 6 varies depending on the frequency f and phase shift; the radiation patterns in the above figures are normalized in magnitude for sake of comparison of their angular distributions.

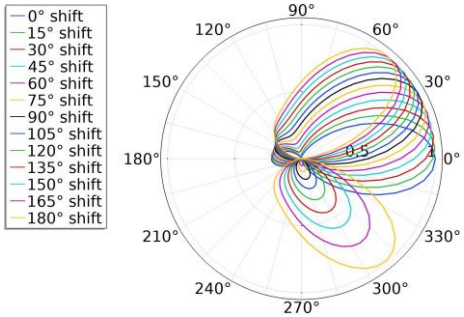

Figure 5: Normalized plot of 2.5 GHz radiation pattern in intended imaging plane (X-Z plane) for various degrees of phase shift. Corresponding plots for frequencies 2.2, 2.3, 2.4 and 2.6 GHz are omitted for brevity but show similar features.

Fig. 5 presents the variation in direction of the main lobe of the radiation pattern as effect of the phase shift $\Delta\phi_{signal}$. As $\Delta\phi_{signal}$ increases the relative radiation intensity increases along the directions opposite the face of the patch (90-270°), as well as along the directions within a secondary lobe to the side of the main lobe. Beyond a certain amount of phase shift, either of these features become large enough that the unidirectionality of the array is undermined by noise from these unwanted directions; as a cutoff metric, this report defines an effective limit $\Delta\phi_{cutoff}$ as the point where $U_{rad,n}(\hat{r})$ in any of these directions exceeds 0.5, or approximately $-3dB$ relative to the maximum.

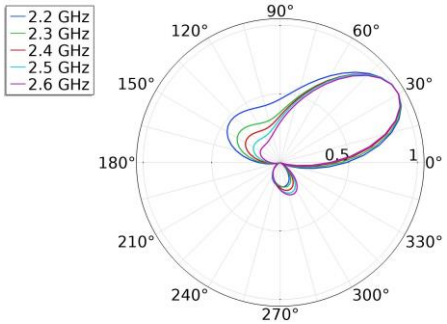

Figure 6: Normalized plot of radiation pattern in intended imaging plane (X-Z plane) with phase shift between elements of $\Delta\phi_{signal}$ = 105°. Corresponding plots for different amount of phase shift are omitted for brevity but show similar frequency-dependence patterns.

As shown in Fig. 6, $U_{rad,n}(\hat{r})$ along the backward directions (90-270° from broadside) is more frequency-sensitive than $U_{rad,n}(\hat{r})$ along the side lobe directions, and reaches the cutoff limit of $U_{rad,n}(\hat{r}) = 0.5$ at lower degrees of phase shift for lower operating frequencies. The radiation pattern along the backward directions reaches cutoff limit at $\Delta\phi_{signal} \approx 105°$ and $f = 2.2$ GHz, corresponding to a maximum off-broadside shift of about 30° and a resultant maximum angular range of 60° for the scanning array when accounting for negative values of phase shift.

4. CONCLUSIONS

The performance of a 2-element phased array was simulated in COMSOL Multiphysics to

assess its viability for use in wideband body-contact radar imaging, wherein the array elements are square patch antennas of polarization perpendicular to the array axis modified with slots for resonance at 2.1 and 2.5 GHz and printed on commercial PCB substrate. The simulated element was found to have a maximum realized gain of 1.87, with a broadside ellipticity of <0.17 indicating mainly linear polarization; however the reflection coefficient magnitude was not low enough to obtain a -10dB impedance bandwidth. It was also found that there is a nonviable band at 2.06-2.14 GHz where the radiation pattern of the basis element deviates from the desired distribution concentrated within a broadside main lobe. The angular range of the scanning array was assessed to be approximately 60°, where the main limiting factor is the potential for noise interference from directions opposite the patch face particularly at lower operating frequencies.

Further research will include modeling the performance characteristics of the antenna element with a layer of impedance-matching material placed over the surface of the antenna trace when the elements are placed in contact with body tissue, to improve transmission efficiency of the signal into the medium of the target region to be imaged while insulating the antenna from the partially conductive medium of the body tissue. Other possible research directions include assessing modified or alternate designs to facilitate an improved range of operating frequencies while maintaining acceptable angular characteristics of the radiation pattern, either by variants of the patch design with closer-spaced resonant frequencies or investigation of alternative geometries of antenna element.

5. ACKNOWLEDGMENTS

The researchers wish to acknowledge the Department of Science and Technology's Philippine Council for Industry, Energy and Emerging Technology Research and Development (DOST-PCIEERD) as funding contributors for the research within which this report is included, as well as the DOST Philippine-California Advanced Research Institutes (PCARI) as funding contributors for the researchers' COMSOL Multiphysics software.

6. REFERENCES

Balanis, C. A. (2016). *Antenna theory - analysis and design.* Hoboken, New Jersey: John Wiley & Sons.

Brovoll, S., Aardal, O., Paichard, Y., Berger, T., Lande, T., & Hamran, S.-E. (2013). Optimal frequency range for medical radar measurements of human heartbeats using body-contact radar. *35th Annual International Conference of the IEEE EMBS* (pp. 1752-1755). Osaka, Japan: IEEE.

Brovoll, S., Berger, T., Paichard, Y., Aardal, O., Lande, T., & Hamran, S.-E. (2014, October). Time-lapse imaging of human heart motion with switched-array UWB radar. *IEEE Transactions on Biomedical Circuits and Systems, 8*(5), 704-715.

Lauteslager, T., Tommer, M., Lande, T. S., & Constandinou, T. G. (2019). Coherent UWB radar-on-chip for in-body measurement of cardiovacular dynamcis. *IEEE Transactions on Biomedical Circuits and Systems, 13*(5), 814-824.

Patel, S. K., & Kosta, Y. (2011). E-shape microstrip patch antenna design for GPS application. *Nirma University International Conference on Engineering.* Ahmedabad, India: IEEE.

Sharma, P., Hui, X., Zhou, J., Conroy, T. B., & Kan, E. C. (2020). Wearable radio-frequency sensing of respiratory rate, respiratory volume and heart rate. *NPJ Digital Medicine*, 98-107.

Wang, Y., Shui, Y., Yang, X., Li, Z., & Wang, W. (2021). Multi-target vital signs detection using frequency-modulated continuous-wave radar. *EURASIP Journal on Advances in Signal Processing*, 103-121.

Yang, F., Zhang, X.-X., Ye, X., & Rahmat-Samii, Y. (2001). Wide-band E-shaped patch antennas for wireless communication. *IEEE Transactions on Antennas and Propagation*, 1094-1100.